



High-temperature plastic deformation of $\langle 110 \rangle$ -oriented BaTiO₃ single crystals

Marion Höfling^{1,2,a)} , Lukas Porz¹ , Michael Scherer¹ , Shuang Gao^{1,3} , Fangping Zhuo¹ , Daniel Isaia¹ , Jürgen Rödel¹ 

¹Department of Materials and Earth Sciences, Technical University of Darmstadt, 64287 Darmstadt, Germany

²Department of Physics, Technical University of Denmark, 2800 Kongens Lyngby, Denmark

³Key Laboratory of Advanced Technologies of Materials (Ministry of Education), School of Materials Science and Engineering, Southwest Jiaotong University, Chengdu 610031, People's Republic of China

^{a)}Address all correspondence to this author. e-mail: marionh@dtu.dk

Jürgen Rödel was an editor of this journal during the review and decision stage. For the JMR policy on review and publication of manuscripts authored by editors, please refer to <http://www.mrs.org/editor-manuscripts/>.

Received: 20 September 2021; accepted: 20 December 2021 published online: 19 January 2022

BaTiO₃ single crystals were deformed in compression along the $\langle 110 \rangle$ crystal axis to study the plastic deformability and dislocation structures at high temperatures under different loading conditions. The yield strength is determined from stress–strain curves under strain rate control, load control, strain rate cycling tests, and under step-wise loading conditions to elucidate the impact of measurement approach in yield strength behavior. A comparison between the chosen methods based on stress-dependent strain rate plots indicates that load control measurements are a suitable alternative to the commonly used strain rate-control experiments in metals. This allows avoiding overloading and providing an estimate of the overall achievable strain rates in a ceramic. Activation energies and activation volumes in the temperature range of 1100–1170 °C indicate a similar mechanical deformation behavior to SrTiO₃.

Introduction

Dislocation-based functionality in ceramics has attracted much attention in recent years. A charged dislocation core and a surrounding space charge layer affect not only ionic and electronic conductivity [1, 2] but also thermal conductivity [3]. Ferroelectric properties can also be affected by dislocations [4]. While dislocations can provide transport routes and scattering centers in dielectric materials, they have the potential to form nucleation and pinning sites for domain walls in ferroelectrics. Domain walls are borders between regions with different spontaneous polarization orientations. Such nucleation and pinning of ferroelectric domain walls at dislocations has been predicted in several simulations [5], leading to a change in ferroelectric and ferroelastic domain structure, polarization, and coercive field (electric field at which domains switch) [6]. Most of these predictions have been experimentally demonstrated only in thin films [7] or around indentations [8]. Recently, plastic deformability for ferroelectric KNbO₃ single crystals has been addressed [9, 10] and the influence of the dislocation imprint at high temperature

on the dielectric and piezoelectric properties of bulk BaTiO₃ has been reported [4].

Both the small number of experimental studies on characterization and affected properties by dislocations in bulk ferroelectrics stem from the difficulty of introducing dislocations without significant sample damage. Therefore, there is still insufficient understanding of dislocation dynamics and high-temperature plasticity that need to be addressed. Some basic understanding of the deformability and dislocation mechanisms in perovskites has been obtained for isostructural SrTiO₃ single crystals. Macroscopic compression experiments from 113 to 1800 K [11–13], and studies on the effect of crystal orientation [12] emphasized a large dislocation-based macroscopic deformability up to several percent [12, 13]. Although the dislocation density can be increased to 10¹³ 1/m², the design and control of dislocation structures are challenging, indicating a complex multiplication and motion mechanism [14].

For BaTiO₃, one of the most widely used ferroelectric model materials with a Curie temperature of 130 °C and a spontaneous

polarization direction of $\langle 001 \rangle$, deformation studies suggest different dislocation- and non-dislocation-based deformation mechanisms depending on experimental conditions [10, 15–19]. In particular, the compression of BaTiO₃ micropillars has attracted attention [20] due to a superelastic behavior [21]. Previously, larger bulk samples have only been deformed in compression under high-temperature creep condition [15, 16, 22]. The activation of the limited slip systems [23], and thus, the movement and multiplication of dislocations depend on the crystallographic orientation of the single crystal [12], covalent and ionic bonds, applied temperature, and stress [13, 24]. Both the $\{110\}\langle 1\bar{1}0 \rangle$ and $\{100\}\langle 001 \rangle$ slip systems can be thermally activated [23], leading to dislocation-controlled deformation. In contrast to metals, in ceramics, not only the lower dislocation density but also its mobility (e.g., 1 $\mu\text{m/s}$) limits high plastic deformation rates [25, 26].

From an experimental point of view, the yield strength is one of the most important characteristic parameters to identify when dislocation-based deformation begins. Near the yield strength, the dislocation density increases rapidly due to an increase in dislocation multiplication rate. The multiplication rate depends on the effective stress and temperature. The stress required for continuous deformation is described as flow stress and changes during the deformation due to, for example, multiple slip, strain hardening, softening, and variation in dislocation multiplication [24, 27].

The measurement approaches and influencing parameters for single-crystal deformation are numerous, i.e., temperature, stress, and strain rate, and therefore, must be carefully selected. The most common experimental parameters are constant strain rate, strain rate cycle (step-wise changes of strain rate), stress relaxation, and creep tests. These methods are used to quantify plasticity and allow the extraction of activation volume, activation energy, and plastic strain rates [28], but their values depend on the choice of method and the active processes [29]. While stress–strain curves recorded with constant strain rate are far more common, control of the loading rate [30, 31] can prevent overloading of the specimen, which is critical for brittle ceramics. Regardless of whether the experiments are under strain rate control or load control, the applied or determined strain rate in most cases is the total strain rate $\dot{\epsilon}_{tot}$ with a superposition of elastic ($\dot{\epsilon}_{elas}$) and inelastic ($\dot{\epsilon}_{inel}$) contributions from the sample.

None of the above-mentioned methods does allow to answer all questions concerning the deformability of ceramic materials by its own. Interestingly, although the deformation phenomena have been studied for selected ceramics such as MgO [27, 30], ZrO₂ [24] and alkali halides [32]; there is still a large gap in knowledge regarding the influence of the chosen plastic deformation experiment type on the yield strength of ceramics. Therefore, this work aims to provide an overview of the evolution of the yield strength and flow stress, as well

as the parameter field for uniaxial compression experiments at high temperatures on the deformability of BaTiO₃ single crystals. We focus on experimental conditions beyond the typical creep parameters to distinguish our work from creep studies and to allow a comparison between different loading conditions. Our overall goal with these experiments is to compare BaTiO₃ with the findings of SrTiO₃ in order to consider, whether both perovskite materials form an isomechanical group. Such isomechanical association is well known for metals (e.g., fcc, bcc, hcp) but has not yet been reported for ceramic materials. To enable such a study, $\langle 110 \rangle$ -oriented BaTiO₃ single crystals were chosen. With this orientation, the dominant $\{100\}\langle 001 \rangle$ slip system can be activated due to the highest possible Schmid factor (m_s) of 0.5 at high temperature. From a mechanistic point of view, the activation volume and activation energy are determined by step-wise loading experiments, as they allow an interpretation of the dislocation mechanism and overall plastic deformation behavior.

Results and discussion

Slip system and dislocations in the deformed sample

Figure 1 summarizes observations by optical microscopy and transmission electron microscopy (TEM) on two representative samples subjected to step-wise deformation to a plastic strain of about 6% at either 1100 °C or 1170 °C. Figure 1a presents a differential interference contrast optical microscopy image of a sample deformed at 1100 °C. Activation of the $\{100\}\langle 001 \rangle$ slip system is demonstrated at one of the $\{100\}$ sides at a 45° angle, similar to the results of Taeri et al. [12] for SrTiO₃. Several samples featured barreling after deformation, which was directly related to the deformation degree. Thus, most of the deformation experiments were stopped in the low percentage range of 1–10%, yet (only minor) microcracking was occasionally noted. An undeformed sample is displayed in Fig. 1b, revealing only ferroelectric domain walls (yellow arrows). Dislocations were observed in both the deformed samples (see TEM images in Fig. 1c–f). The TEM images provide an overview of different but common dislocation features (white arrows) and domain walls (yellow arrows) in deformed BaTiO₃ single crystals. The mesoscopic arrangement varies locally from straight dislocations passing through domain walls (c) and (d), to dislocation loops (e)–(f). With increasing deformation temperature from 1100 to 1170 °C, dislocation loops or dislocation loop segments were observed more often than straight dislocations [marked individually in (e)–(f)], indicating that dislocation configuration can be tuned by changing the deformation conditions.

Evaluation of the yield strength

As loading under strain rate control is common in metals and has also been applied to characterize single crystal SrTiO₃ [12,

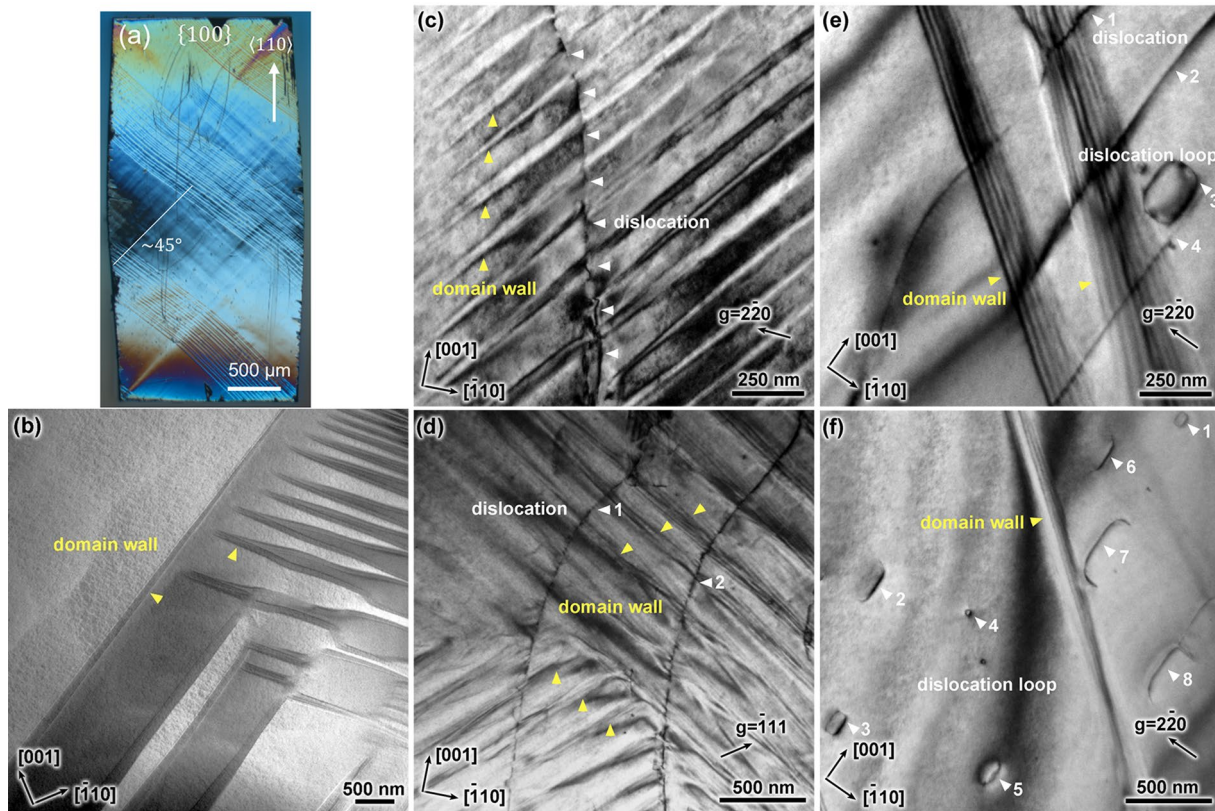


Figure 1: (a) Differential interference contrast optical image of a 6% deformed sample at 1100 °C. The straight features at an angle of about 45° are related to the plastic deformation. (b) BF STEM image of a reference-undeformed BaTiO₃ sample. (c–d) Two beam condition BF images of the dislocation structures deformed at 1100 °C and (e, f) deformed at 1170 °C. The g vector is given in (c–f).

33], this method was chosen as the starting point for quantification of the yield strength. Changes in strain rate reveal the stress dependence of the strain rate tested at initial strain rates of 10⁻⁵ 1/s and 10⁻⁴ 1/s, as presented in Fig. 2a. Both strain rates were alternately applied for three times. Quantification

of the extracted $\sigma_{p0.2}$ (Fig. 2b) illustrates that a higher $\sigma_{p0.2}$ is required for the faster deformation. As the number of strain rate cycles increases, a stabilization of the $\sigma_{p0.2}$ values was observed (Fig. 2b). For 10⁻⁵ 1/s, a pronounced yield point is noted in Fig. 2a (black), which increases from 40 to 60 MPa from the first

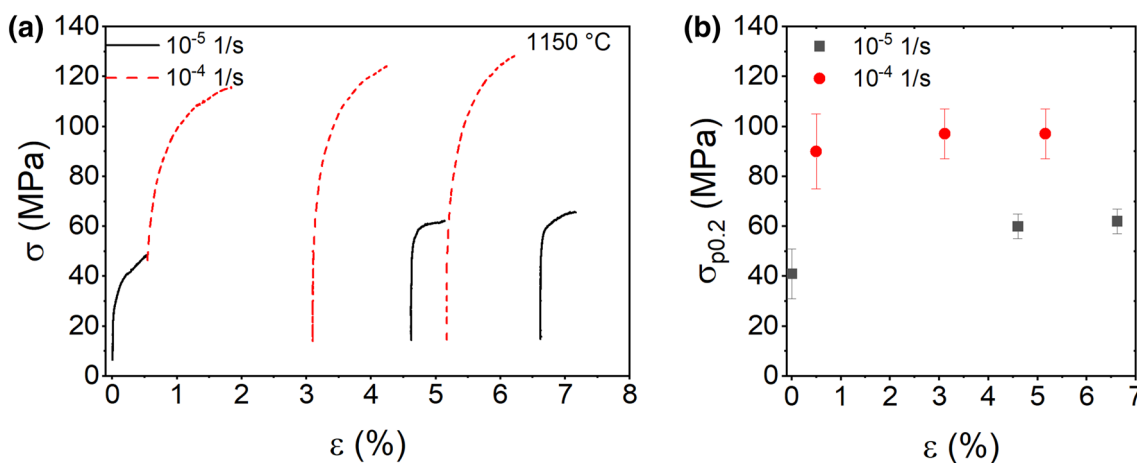


Figure 2: Strain rate cycling test with alternating initial strain rates of 10⁻⁵ 1/s and 10⁻⁴ 1/s represented as stress–strain curves in (a) and $\sigma_{p0.2}$ values dependent on strain rate in (b).

to the second and third deformation steps at the same strain rate. This is suggested to indicate strain hardening [34]. In contrast to 10^{-5} 1/s, the yield point is less pronounced during deformation at 10^{-4} 1/s and increases only slightly with increasing degree of deformation, which underlines that the yield strength at 10^{-4} 1/s is quasi-independent of previous history of the sample and the actual degree of deformation, which is above 5% for the third cycle.

As the BaTiO₃ single-crystal samples exhibit pronounced strain rate sensitivity at 1150 °C, we investigated how this material behaves under different loading conditions.

To this end, stress–strain curves for (a) initial strain rate-control, (b) load control, and (c) load control experiments at different temperatures are presented in Fig. 3, with each measurement starting with an undeformed single crystal. All measurements were stopped in the range of 2–10% deformation to avoid fatal failure.

In the first step, initial strain rate-control experiments were recorded (Fig. 3a) and the resulting loading rate was determined as function of time (Fig. S1). Similar to the strain rate cycling tests, an increase in strain rate prompts a higher $\sigma_{p0.2}$. Further, flow stresses at a deformation level of 3% increase with faster deformation. In terms of loading rate, a level of 20 N/s is required at the yield strength at 5×10^{-4} 1/s. With increasing time, the loading rate decreases (Fig. S1). A different behavior is observed for 10^{-5} 1/s, where the resulting loading rate is almost constant at 0.2 N/s. Due to the combination of low initial dislocation density and low dislocation velocity [35], high initial strain rates can initially result in a sharp increase in applied load, as seen here for the 5×10^{-4} 1/s measurement. This stress peak results from the difficulty of initially multiplying and moving the dislocations to meet the specified initial total strain rate $\dot{\epsilon}_{tot}$ —a challenge not commonly encountered in metals. For higher strain rates, such a stress peak may lead to sample failure by initiating crack growth.

In the second step, load control experiments were conducted to avoid stress peaks, presented in Fig. 3b, and to determine an optimum strain rate (Fig. S2). Stress values increase with increasing loading rate for both $\sigma_{p0.2}$ and the flow stress (e.g., at 3% deformation). While 3% total deformation is already reached below 100 MPa for the 0.5 N/s measurement, almost 200 MPa are required for the 5 N/s loading rate. Due to higher loading rate, strain rate also increases drastically, as quantified in Fig. S2a, e.g., from 10^{-6} for 0.5 N/s to 10^{-4} for 5 N/s after 100 s, corresponding to a strain of <0.01% and 1.8%, respectively (Fig. S2b). When the 0.5 N/s measurement is stopped at approximately 3% deformation, the achieved strain rate is in the range of 10^{-4} 1/s, which agrees well with the results of the strain rate-control measurements.

Figure 3c depicts the temperature-dependent deformation behavior at a loading rate of 2 N/s and a temperature range from

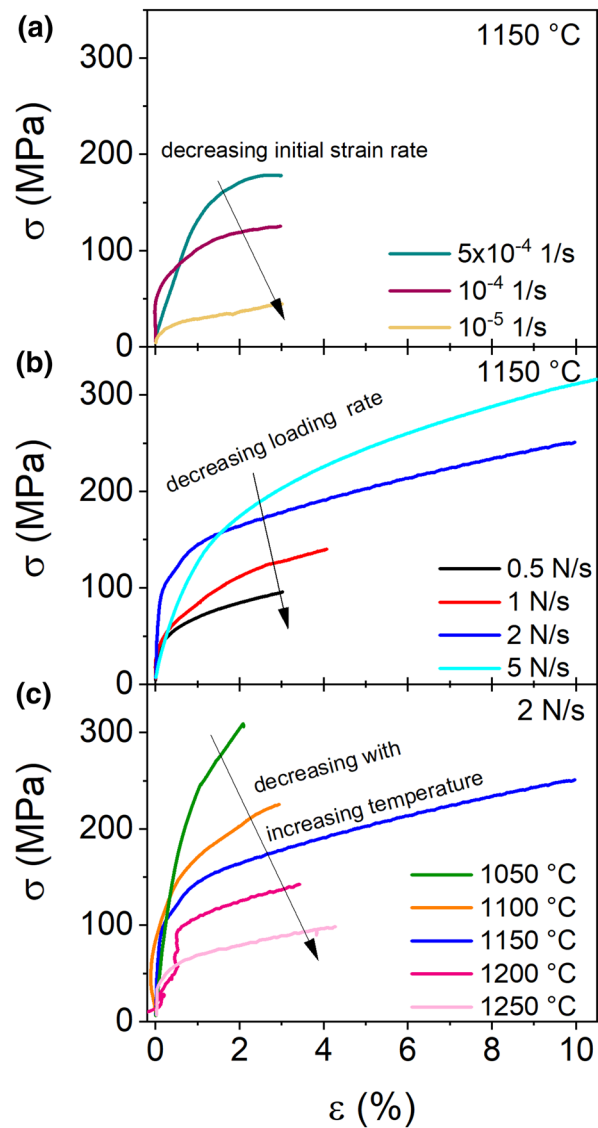


Figure 3: (a) Initial strain rate-control and (b) loading rate-control experiments at 1150 °C. (c) Temperature-dependent stress–strain curves at 1050 °C, 1100 °C, 1150 °C, 1200 °C, and 1250 °C, obtained at 2 N/s.

1050 to 1250 °C. As the temperature increases, $\sigma_{p0.2}$ and the stress required decrease, while the effective strain rate increases (see Fig. S2c, d). A more detailed comparison of the characteristic values follows in the discussion section.

Discussion: stress–strain curves

The effect of loading condition and temperature on yield strength $\sigma_{p0.2}$ and the slope and shape of the stress–strain curves are discussed below.

Figure 4 features a similar trend, $\sigma_{p0.2}$ increases with increasing initial strain rate (a) and loading rate (b) but decreases with increasing temperature (c).

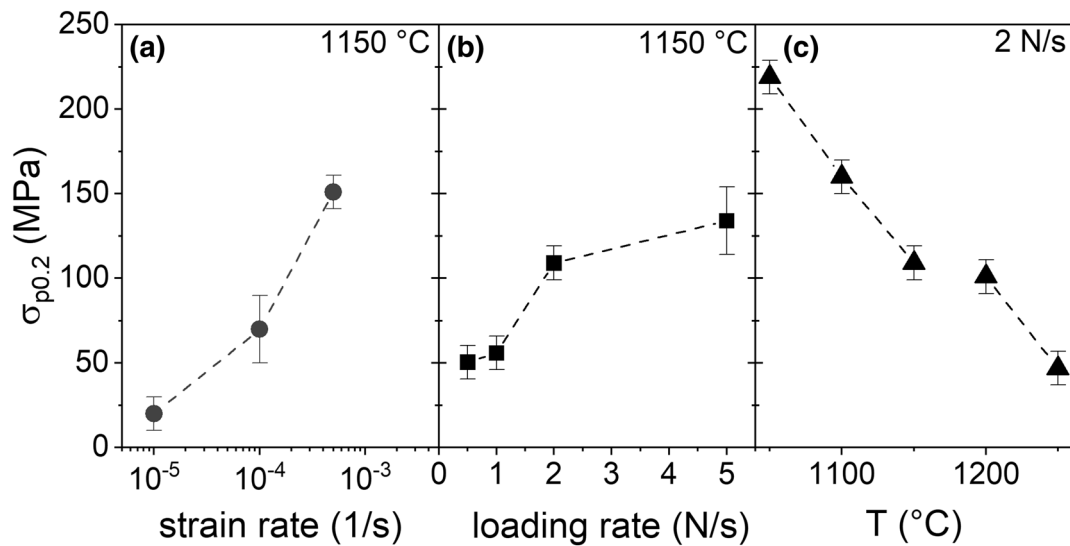


Figure 4: Critical compressive stress as function of loading condition at 1150 °C (a, b) and temperature (c).

$\sigma_{p0.2}$ varies from 20 MPa for 10^{-5} 1/s, 70 MPa for 10^{-4} 1/s to 150 MPa for 5×10^{-4} N/s, corresponding to a tenfold and 50-fold increase in strain rate and a threefold or sevenfold increase in $\sigma_{p0.2}$, respectively. Such a strong strain rate dependence of $\sigma_{p0.2}$ was observed in the strain rate cycling test, signifying a changing dislocation structure and variations in dislocation density. Changes in yield strength gained for the two different strain rate-control methods, e.g., $\sigma_{p0.2} = 70$ MPa (Fig. 4a) and 90–97 MPa for the strain rate cycling test, can be rationalized by slight tilting of the sample during compression and sample-to-sample variation. For SrTiO₃, stresses in the range of 90 MPa were reported for a strain rate of 10^{-4} 1/s at 1141 °C [12], which is in the same range as the results for BaTiO₃. These stress and strain rate values are well above the creep experiment on BaTiO₃ single crystals, where 25.2 MPa were applied at 1151 °C, reaching a creep strain rate of 2.1×10^{-7} 1/s. [16].

The selected load control conditions (Fig. 4a) require at least 50 MPa to reach the yield strength at 0.5 N/s and increase to 135 MPa at 5 N/s, which implies a threefold increase in $\sigma_{p0.2}$ for a tenfold increase in loading rate. This indicates either that BaTiO₃ has a loading rate sensitivity of $\sigma_{p0.2}$ or may feature a delayed yield at 1150 °C. When the dislocation multiplication requires longer time spans, than it is likely that the system has already applied much more load than actually necessary until a change in the multiplication can have an impact [36]. Above $\sigma_{p0.2}$, the flow stress increases continuously, indicating strain hardening. Such a strong dependence between loading rate and yield strength was not observed in MgO [30], where only the flow stress was strongly affected by the increase in loading rate. This difference in $\sigma_{p0.2}$ could be related to different

applied temperature (1321 °C for MgO), differences in crystal structure, slip system, low yield strength of 0.03 MPa (0.004 psi), and higher dislocation mobility in MgO [30]. An increase in loading rate results in an increase in strain rate with time (see Fig. S2a). Corresponding total strain rates easily reach values above 10^{-4} 1/s at high loading rates, which is in the upper range of strain rate-control compression experiments on oxides [12, 33]. Note that due to the changing strain rate, the relatively high degree of deformation and the tendency to barreling (see Fig. 1a), the steady-state deformation condition cannot be used to interpret the data as the dislocation structure and density are not constant [37]. Although it is unclear how large the contribution of plastic strain rate is, the results point towards a dislocation-driven deformation mechanism with dislocation multiplication and an increase in mobile dislocation density, as indicated in the TEM images (Fig. 1c–f). Dislocation movement is a thermally activated process, which is reflected in the temperature-dependent $\sigma_{p0.2}$ in Fig. 4c. An increase from 1050 to 1250 °C causes a reduction of $\sigma_{p0.2}$ from 220 to 50 MPa for a loading rate of 2 N/s. Taeri et al. [12] reported for SrTiO₃ a decrease of 250 MPa (at 982 °C) to 90 MPa (at 1141 °C) with a strain rate of 10^{-4} 1/s. This temperature trend is confirmed for several other ceramic materials and loading conditions such as SrTiO₃ [12, 13] (initial strain rate), ZrO₂ [38] (initial strain rate), and MgO [39] (load rate control).

The increase of strain rate with increasing temperature follows an Arrhenius type behavior (see Eq. 1) and quantifies higher dislocation mobility.

$$\dot{\epsilon} = \dot{\epsilon}_0 \exp\left(-\frac{\Delta G^*}{k_B T}\right) \quad (1)$$

with $\dot{\epsilon}_0$ as prefactor, ΔG^* as activation energy, k_B as Boltzmann constant and T as temperature, independent of the type of deformation experiment.

Quantification of the deformability

The objective of this section is to determine strain rate maps (strain rate as a function of stress), activation energy, and activation volume to interpret the deformation mechanism.

To this end, step-wise stress experiments were conducted at a given temperature (Fig. 5a) with intermittent constant loading rate of 2 N/s. The stresses applied here are much higher than applied in creep experiments (< 25 MPa) for BaTiO₃ [16] to distinguish between creep and flow. In order to assess the stress dependence, the data featured in Fig. 5a are divided into dynamic measurements (component of constant loading rate, similar to Fig. 3b) and static measurements, where the stress is held constant for several minutes (similar to creep tests).

Plotting the corresponding strain rate as function of applied stress affords construction of a strain rate map, presented in Fig. 5b with lines (dynamic) and circles (static). Such a map informs on the rate of the deformation process at a given stress level and the required stress in strain rate-control experiments and vice versa. The results indicate that load control (dynamic) measurements can provide comparable strain rates to the typical step-wise stress measurements, like in creep studies. In such tests, the stress is held constant and the change in strain is measured as a function of time, see e.g., [16, 40].

A detailed comparison of the different measurement approaches is presented in Fig. 5b. Four types of data are plotted in the same graph: (1) The yield strength recorded with strain rate control and (2) the values recorded with loading rate control. (3) The strain rate values extracted from step-wise constant

stress measurements, and (4) continuous lines for dynamic loading with loading rate control. All data points coincide well, suggesting that all four approaches give comparable results. This allows at least for an initial screening—selecting the easiest mechanical testing approach. The full strain rate maps for the load control, initial strain rate control, and temperature-dependent load control experiments from Fig. 3 are featured in Fig. 3. Beyond a certain point (~ 100 MPa), applying a higher stress results only in a small increase in strain rate. Such a flattening of the strain rate as a function of the stress curve is rarely reported in metals at elevated temperatures.

In the next step, we analyze the influence of the stress levels in combination with the temperature on the activation energy and the activation volume. The apparent activation energy (ΔG^* , Eq. 1) and activation volume (V_A , Eq. 2) were determined based on the temperature-dependent step-wise stress data presented in Fig. 5. Both equations contain a term for the strain rate, the Boltzmann constant k_B , and the applied shear stress τ ($\tau = m_s^* \sigma$).

$$V_A(\tau) = k_B T \left(\frac{\partial \ln(\dot{\epsilon} * 1s)}{\partial \tau} \right)_T. \quad (2)$$

While all stress levels reveal a similar slope at high temperature, the slopes vary considerably at lower temperature. These trends suggest that the stress sensitivity, and thus, the deformation mechanisms, varies with temperature (Fig. 6a). The activation energy of the deformation mechanisms is correlated to the slope in Fig. 6a. The respective values of the activation energy are presented in Fig. 6b as a function of applied stress level and temperature range. In the temperature range between 1100 and 1150 °C, considerable stress dependence leads to pronounced differences in activation energies of 10.8 eV for 50 MPa and 4.2 eV for 100 MPa. In contrast, the activation energy is

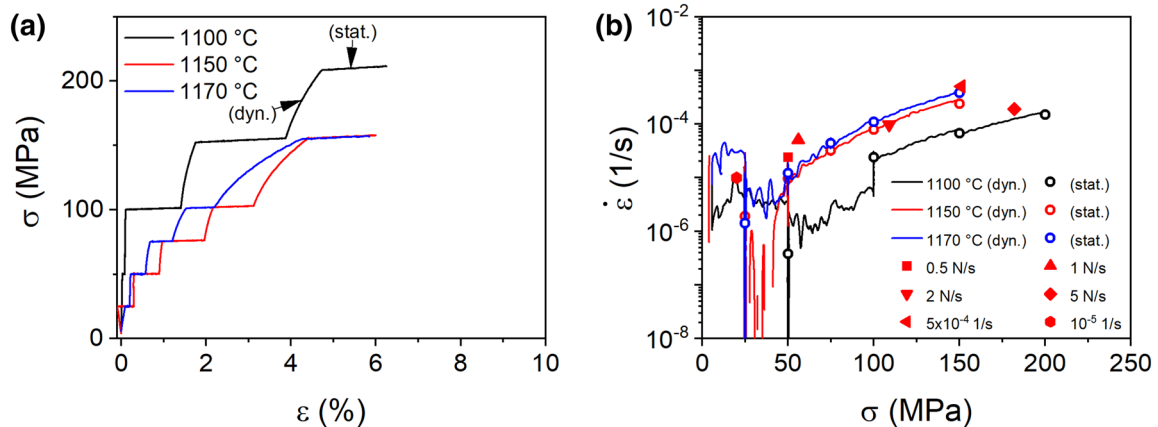


Figure 5: (a) Stress–strain curve as function of temperature and stress level (stat.) loading condition 2 N/s. (b) Strain rate as function of the applied compressive stress. Data from (a) are represented as lines in (b). The continuous increase in load is indicated with straight lines (dyn.), strain rates determined at the stress plateau in (a) are highlighted with circles (stat.). Strain rates at the $\sigma_{p0.2}$ values of the data in Fig. 2 are presented as red symbols. Absolute strain values were smoothed with the Savitzky-Golay method before and after the strain rate was determined.

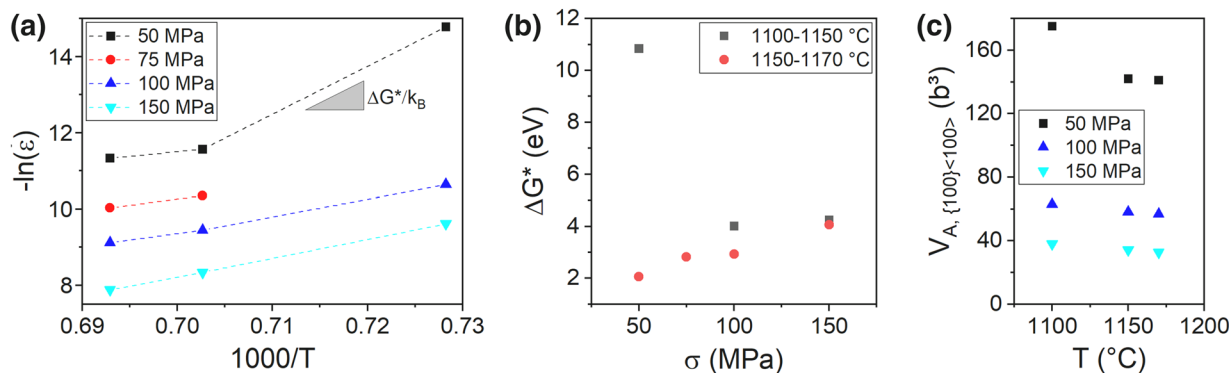


Figure 6: (a) Strain rate dependence as function of temperature to determine the (b) apparent activation energy from the slope in (a), and the activation volume (c).

with 2.1–4.1 eV almost independent of stress in the temperature range from 1150 to 1170 °C. At 4.1 eV at 150 MPa, the data are within the range of the climb-controlled mechanism (4.9 eV) reported by Beauchesne et al. [16] for creep experiments on BaTiO₃ single crystals at higher temperatures. Note that ¹³¹Ba diffusion (3.6 eV) is in a similar range, suggesting that Ba is the rate-controlling cation of the mechanism [41, 42], which would support that a non-conservative dislocation mechanism like climb is involved. Since the activation energy alone can include both dislocation-based and diffusion-based mechanisms, an inspection of the activation volume is recommended. The activation volume is in the range of 140–175b³ at low stresses (50 MPa), reaching 33–38b³ at higher stresses, under the assumption that the predominant high-temperature {100}(001) slip system is active (see Fig. 6c). The large activation volume at 50 MPa can be rationalized by the fact that $\sigma_{p0.2}$ is not yet reached for this loading condition. Above $\sigma_{p0.2}$, the activation volume decreases considerably. At 150 MPa our results of about 35 to 40b³ compare favorably with the value of 30b³ at 1177 °C presented by Taeri et al. [12] for the same single-crystal orientation in SrTiO₃.

Comparison of the deformation behavior of BaTiO₃ and SrTiO₃

In the last section, we compare BaTiO₃ with SrTiO₃ to probe whether these two materials behave isomechanically. Plotting the strain rate against the applied stress (Fig. 7) allows us to capture the deformation behavior over a wide range of stresses and also over several orders of magnitude of strain rate. Both perovskite materials, (110)-oriented Fe-doped SrTiO₃ evaluated at 1100 °C and 1150 °C (at constant stress) and (110)-oriented BaTiO₃ at 1100 °C, 1150 °C, and 1170 °C (load control at 2 N/s), behave in similar fashion at high temperature. Below 75 MPa, the strain rate increases sharply with increasing stress, indicating high stress sensitivity for both materials. The slope for both materials decreases with increasing stress and reaches a limit of

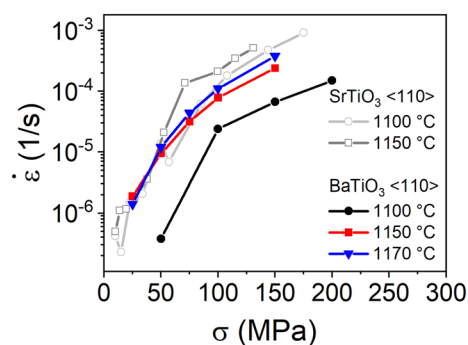


Figure 7: Comparison of the deformation behavior in BaTiO₃ and Fe-doped SrTiO₃ under similar conditions.

about 10⁻³ 1/s in strain rate (unpublished data). Since for both materials, the yield strength is in the range of ~80–120 MPa, depending on loading conditions [12], the change in slope may be associated with a change in deformation mechanism. At high stresses, the activation volume for both materials is close to the values expected for the kink-pair mechanism, suggesting it as the dominant mechanism at high stresses at 1150 °C. Nevertheless, it should be noted that the temperature sensitivity is less pronounced for the Fe-doped SrTiO₃ than for BaTiO₃. This may indicate that BaTiO₃ and SrTiO₃ behave in isomechanical fashion in principle, but that BaTiO₃ requires slightly higher temperature for the same behavior, e.g., due to different bond strength, dislocation core structure, and mesoscopic dislocation structure [14].

Conclusions

The yield strength and the flow stress of (110)-oriented BaTiO₃ single crystals mainly depend on temperature and little on the selected loading conditions. Mechanical testing under load control, which is uncommon in metals, features similar trends in yield strength as testing under strain rate control for this perovskite and is, therefore, seen as complementary. By comparing

a total of four different loading methods, the values of yield strength were quantified in the range of 20 MPa and 220 MPa. Slower deformation and higher temperature lead to lower $\sigma_{p0.2}$ and less sample damage such as cracking and spallation, regardless of the parameter type (loading rate or strain rate) selected. Strain rate as function of stress plots was used to highlight a flattening of the curve at high stresses. As result, a change in deformation mechanism but also a maximum achievable strain rate is indicated. Activation energies in the range of 2–11 eV and activation volumes of 33–175b³ in a stress range of 50–150 MPa and 1100 °C to 1170 °C suggest an isomechanical behavior for BaTiO₃ and SrTiO₃ at high stresses.

Materials and methods

Deformation experiments were carried out on polished high-purity top-seeded solution-grown BaTiO₃ single crystals (FEE GmbH, a division of Electro-Optics Technology GmbH, Germany). The purchased single crystals were cut into [110]-oriented samples with a dimension of 2 × 2 × 4 mm³ and loaded along the 4 mm axis. Compression experiments were conducted using two mechanical loading frames for different temperatures. For temperatures below 1200 °C, a load frame (Z010, Zwick GmbH & Co. KG, Germany) equipped with an integrated furnace (LK/SHC 1500–85-150-1 V-Sonder, HTM Reetz GmbH, Germany) and a linear variable differential transducer (LVDT) for precise displacement measurements was utilized. Measurements at 1200 °C and 1250 °C were performed using silicon carbide-based dies and a load frame (2850-30kN Instron, Instron, USA) equipped with a HTM Reetz furnace, a 30 kN test fixture, and a LVDT.

Twenty crystals were deformed to several percent. The aim of these measurements was to evaluate the influence of the applied loading rate, strain rate, strain rate cycling tests, and step-wise stress tests on the measured yield strength at different temperatures. In addition, the step-wise stress tests were used to determine the activation energy and activation volume of the deformation process at hand. The single crystals were deformed under load control (0.5 N/s, 1 N/s, 2 N/s, and 5 N/s), initial strain rate control (10⁻⁵ 1/s, 10⁻⁴ 1/s, and 5 × 10⁻⁴ 1/s) or alternating strain rate control (10⁻⁵ 1/s, 10⁻⁴ 1/s) at 1150 °C. During the alternating measurements, the strain rate alternated between 10⁻⁵ 1/s and 10⁻⁴ 1/s three times.

The range of load control experiments is approximately 0.15–1.5 MPa/s, leading to strain rates of 10⁻⁶ 1/s to 10⁻³ 1/s, which are, thus, higher than in typical creep experiments [16]. They cover a slightly larger range than the initial strain rate-control experiments. A comparison with the behavior of MgO (0.18–1.14 MPa/s) is also afforded [30]. Preliminary experiments indicated that too high strain rates can cause temporary overload for materials with

low dislocation density, which can lead to fracture of the sample [35]. Therefore, we opted for load control compression to allow for a sufficient time period for dislocation nucleation and to identify feasible strain rates, although the load control method is uncommon for metals where dislocation density and multiplication are less critical than in ceramics [24, 43]. The strain rate-control experiments, or more precisely, the displacement control experiments, were again performed at higher strain rates than typical for creep deformation studies. With a variation in strain rate of 10× and 50×, the chosen strain rates are in a similar range as in another perovskite study on SrTiO₃ [12, 33]. Strictly speaking, then, there are no well-defined strain rates at higher strains in displacement control experiments as only the sum of elastic and inelastic strain rate is controlled. Hence, the term “initial strain rate” is used. Further compression experiments were conducted at 1050 °C, 1100 °C, 1200 °C, and 1250 °C with a loading rate of 2 N/s. This temperature range overlaps with the range investigated for SrTiO₃, allowing comparison of the yield strength $\sigma_{p0.2}$ (defined here as stress at 0.2% plastic strain in compression) and the consideration of the isomechanical behavior [12]. The influence of temperature and stress was investigated with step-wise stress experiments (similar to step-wise creep tests [28] but at higher stresses) for 1100 °C, 1150 °C, and 1170 °C at stresses between 25 and 200 MPa. The stress was kept constant at each stress level (static) for several minutes, with intermittent load increase of 2 N/s between the stress levels (dynamic), respectively. In order to maintain the absolute deformation strain in the low percentage range, the holding time at the different stress levels was decreased with increasing stress and temperature.

Optical microscopy was performed using a 3D-Laser scanning microscope (LEXT OLS4100, Olympus, Shinjuku, Japan) in differential interference contrast mode (U-DIC) and a polarizer.

Bright field transmission electron microscopy (BF-TEM) and scanning TEM (STEM) images were taken by a JEOL-2100F TEM (Jeol, Akishima, Japan). Single crystals were cut after step-wise stress experiments at 1100 °C and 1170 °C perpendicular to the deformation direction into slices of 300 μm in thickness. The slices were polished using diamond-lapping film with grain sizes of 9, 6, 3, and 1 μm, respectively, and finally thinned to 20 μm. In order to release the accumulated strain during polishing, the slices were afterwards annealed at 200 °C for 30 min with a heating and cooling rate of 1 °C/min. Resulting TEM slices were mounted on a supporting molybdenum grid (100 mesh) and thinned by argon ion (Gatan model 600 dual ion mill) into electron transparency.

Acknowledgments

The authors would like to thank Patrick Breckner for supporting the Instron loading frame set up. Furthermore, SG thanks H.-J. Kleebe for access to the TEM.

Author contributions

MH, FZ, and MS conducted the deformation experiments. MH analyzed the deformation results. SG performed TEM. MS and DI built the loading frame. MH, LP, MS, and JR discussed the deformation data and interpreted together with SG and FZ the TEM results. All coauthors contributed to the manuscript.

Funding

Open Access funding enabled and organized by Projekt DEAL. This work was supported by project No. 414179371 of the German Research Foundation (DFG). F. Z. would like to thank the Alexander von Humboldt Foundation for financial support.

Data availability

The data that support the findings of this study are available from the corresponding author upon reasonable request.

Code availability

Not applicable.

Declarations

Conflict of interest The authors declare that there is no conflict of interest.

Open Access

This article is licensed under a Creative Commons Attribution 4.0 International License, which permits use, sharing, adaptation, distribution and reproduction in any medium or format, as long as you give appropriate credit to the original author(s) and the source, provide a link to the Creative Commons licence, and indicate if changes were made. The images or other third party material in this article are included in the article's Creative Commons licence, unless indicated otherwise in a credit line to the material. If material is not included in the article's Creative Commons licence and your intended use is not permitted by statutory regulation or exceeds the permitted use, you will need to obtain permission directly from the copyright holder. To view a copy of this licence, visit <http://creativecommons.org/licenses/by/4.0/>.

Supplementary Information

The online version contains supplementary material available at <https://doi.org/10.1557/s43578-022-00485-6>.

References

1. R.W. Whitworth, *Adv. Phys.* **24**(2), 203–304 (1975). <https://doi.org/10.1080/00018737500101401>
2. K. Szot, C. Rodenbücher, G. Bihlmayer, W. Speier, R. Ishikawa, N. Shibata, Y. Ikuhara, *Crystals* **8**(6), 241 (2018). <https://doi.org/10.3390/cryst8060241>
3. S.I. Kim, K.H. Lee, H.A. Mun, H.S. Kim, S.W. Hwang, J.W. Roh, D.J. Yang, W.H. Shin, X.S. Li, Y.H. Lee, *Science* **348**(6230), 109–114 (2015). <https://doi.org/10.1126/science.aaa4166>
4. M. Höfling, X. Zhou, L.M. Riemer, E. Bruder, B. Liu, L. Zhou, P.B. Groszewicz, F. Zhuo, B.-X. Xu, K. Durst, X. Tan, D. Damjanovic, J. Koruza, J. Rödel, *Science* **372**(6545), 961 (2021). <https://doi.org/10.1126/science.abe3810>
5. A. Kotsos, C.M. Landis, *Int. J. Solids Struct.* **46**(6), 1491–1498 (2009). <https://doi.org/10.1016/j.ijsolstr.2008.11.021>
6. H.H. Wu, J. Wang, S.G. Cao, L.Q. Chen, T.Y. Zhang, *Smart Mater. Struct.* **23**(2), 7 (2014). <https://doi.org/10.1088/0964-1726/23/2/025004>
7. P. Gao, C.T. Nelson, J.R. Jokisaari, S.H. Baek, C.W. Bark, Y. Zhang, E.G. Wang, D.G. Schlom, C.B. Eom, X.Q. Pan, *Nat. Commun.* **2**(591), 1–6 (2011). <https://doi.org/10.1038/ncomms1600>
8. G.A. Schneider, T. Scholz, J. Muñoz-Saldana, M.V. Swain, *Appl. Phys. Lett.* **86**(19), 3 (2005). <https://doi.org/10.1063/1.1920410>
9. A.F. Mark, M. Castillo-Rodríguez, W. Sigle, *J. Eur. Ceram. Soc.* **36**(11), 2781–2793 (2016). <https://doi.org/10.1016/j.jeurceramsoc.2016.04.032>
10. M. Höfling, M. Trapp, L. Porz, H. Uršič, E. Bruder, H.-J. Kleebe, J. Rödel, J. Koruza, *J. Eur. Ceram. Soc.* **41**(7), 4098–4107 (2021). <https://doi.org/10.1016/j.jeurceramsoc.2021.02.023>
11. M. Castillo-Rodríguez, W. Sigle, *Scr. Mater.* **64**(3), 241–244 (2011). <https://doi.org/10.1016/j.scriptamat.2010.10.014>
12. S. Taeri, D. Brunner, W. Sigle, M. Rühle, *Z. Metallk.* **95**(6), 433–446 (2004). <https://doi.org/10.3139/146.017984>
13. D. Brunner, S. Taeri-Baghdadani, W. Sigle, M. Rühle, *J. Am. Ceram. Soc.* **84**(5), 1161–1163 (2001). <https://doi.org/10.1111/j.1151-2916.2001.tb00805.x>
14. L. Porz, T. Frömling, A. Nakamura, N. Li, R. Maruyama, K. Matsunaga, P. Gao, H. Simons, C. Dietz, M. Rohnke, J. Janek, J. Rödel, *ACS Nano* **15**(6), 9355–9367 (2021). <https://doi.org/10.1021/acsnano.0c04491>
15. N. Doukhan, J.C. Doukhan, *Phys. Chem. Minerals* **13**(6), 403–410 (1986). <https://doi.org/10.1007/BF00309185>
16. S. Beauchesne, J.P. Poirier, *Phys. Earth Planet. Inter.* **55**(1), 187–199 (1989). [https://doi.org/10.1016/0031-9201\(89\)90242-2](https://doi.org/10.1016/0031-9201(89)90242-2)
17. K. Edalati, M. Arimura, Y. Ikoma, T. Daio, M. Miyata, D.J. Smith, Z. Horita, *Mater. Res. Lett.* **3**(4), 216–221 (2015). <https://doi.org/10.1080/21663831.2015.1065454>
18. O. Eibl, P. Pongratz, P. Skalicky, H. Schmelz, *Phys. Status Solidi A* **108**(2), 495–502 (1988). <https://doi.org/10.1002/pssa.2211080203>
19. T. Suzuki, M. Ueno, Y. Nishi, M. Fujimoto, *J. Am. Ceram. Soc.* **84**(1), 200–206 (2001). <https://doi.org/10.1111/j.1151-2916.2001.tb00631.x>

20. N.G. Mathews, A.K. Saxena, C. Kirchlechner, G. Dehm, B.N. Jaya, *Scr. Mater.* **182**, 68–73 (2020). <https://doi.org/10.1016/j.scriptamat.2020.02.039>
21. Y. Li, K. Chu, C. Liu, P. Jiang, K. Qu, P. Gao, J. Wang, F. Ren, Q. Sun, L. Chen, J. Li, *Proc Nat Acad Sci* **118**(24), e2025255118 (2021). <https://doi.org/10.1073/pnas.2025255118>
22. P.R. Ren, M. Hoefling, J. Koruza, S. Lauterbach, X.J. Jiang, T. Fromling, D.K. Khatua, C. Dietz, L. Porz, R. Ranjan, H.J. Kleebe, J. Rödel, *J. Am. Ceram. Soc.* **103**(3), 1891–1902 (2020). <https://doi.org/10.1111/jace.16881>
23. J.P. Poirier, S. Beauchesne, F. Guyot, Deformation mechanisms of crystals with perovskite structure, in *Perovskite: A Structure of Great Interest to Geophysics and Materials Science*. ed. by A. Navrotsky, D.J. Weidner (American Geophysical Union, Washington, DC, 1989). <https://doi.org/10.1029/GM045p0119>
24. U. Messerschmidt, Dislocation dynamics during plastic deformation, in *Springer Series in Materials Science*. (Springer, Berlin, Heidelberg, 2010). <https://doi.org/10.1007/978-3-642-03177-9>
25. L. Porz, in Technical University of Darmstadt, tprints:17954, (2021)
26. K. Sumino, I. Yonenaga, M. Imai, T. Abe, *J. Appl. Phys.* **54**(9), 5016–5020 (1983). <https://doi.org/10.1063/1.332770>
27. J. Amodeo, S. Merkel, C. Tromas, P. Carrez, S. Korte-Kerzel, P. Cordier, *J. Chevalier, Crystals* **8**(6), 240 (2018). <https://doi.org/10.3390/cryst8060240>
28. A.G. Evans, R.D. Rawlings, *Phys. Status Solidi* **34**(1), 9–000 (1969). <https://doi.org/10.1002/pssb.19690340102>
29. W. Blum, P. Eisenlohr, F. Breutinger, *Metall. Mater. Trans. A* **33**(2), 291–303 (2002). <https://doi.org/10.1007/s11661-002-0090-9>
30. S.M. Copley, J.A. Pask, *J. Am. Ceram. Soc.* **48**(3), 139–146 (1965). <https://doi.org/10.1111/j.1151-2916.1965.tb16050.x>
31. C.O. Hulse, S.M. Copley, J.A. Pask, *J. Am. Ceram. Soc.* **46**(7), 317–323 (1963). <https://doi.org/10.1111/j.1151-2916.1963.tb11738.x>
32. W.G. Johnston, J.J. Gilman, *J. Appl. Phys.* **30**(2), 129–144 (1959). <https://doi.org/10.1063/1.1735121>
33. E.A. Patterson, M. Major, W. Donner, K. Durst, K.G. Webber, J. Rödel, *J. Am. Ceram. Soc.* **99**(10), 3411–3420 (2016). <https://doi.org/10.1111/jace.14352>
34. J. Chakrabarty, *Applied Plasticity*, 2nd edn. (Springer, New York, 2010). <https://doi.org/10.1007/978-0-387-77674-3>
35. W.G. Johnston, *J. Appl. Phys.* **33**(9), 2716–2730 (1962). <https://doi.org/10.1063/1.1702538>
36. J.J. Gilman, W.G. Johnston, Dislocations in lithium fluoride crystals, in *Solid State Physics*, vol. 13, ed. by F. Seitz, D. Turnbull (Academic Press Inc, Cambridge, 1962). [https://doi.org/10.1016/S0081-1947\(08\)60457-9](https://doi.org/10.1016/S0081-1947(08)60457-9)
37. W. Blum, *Scr. Mater.* **146**, 27–30 (2018). <https://doi.org/10.1016/j.scriptamat.2017.10.029>
38. B. Baufeld, M. Bartsch, U. Messerschmidt, D. Baither, *Acta Metall Mater.* **43**(5), 1925–1933 (1995). [https://doi.org/10.1016/0956-7151\(94\)00400-C](https://doi.org/10.1016/0956-7151(94)00400-C)
39. J. Amodeo, P. Carrez, B. Devincere, P. Cordier, *Acta Mater.* **59**(6), 2291–2301 (2011). <https://doi.org/10.1016/j.actamat.2010.12.020>
40. J.-P. Poirier, *Creep of Crystals: High-Temperature Deformation Processes in Metals, Ceramics and Minerals* (Cambridge University Press, Cambridge, 1985). <https://doi.org/10.1017/CBO9780511564451>
41. M.-H. Lin, J.-F. Chou, H.-Y. Lu, *J. Eur. Ceram. Soc.* **20**(4), 517–526 (2000). [https://doi.org/10.1016/S0955-2219\(99\)00174-0](https://doi.org/10.1016/S0955-2219(99)00174-0)
42. L.A. Xue, Y. Chen, E. Gilbert, R.J. Brook, *J Mater Sci* **25**(2), 1423–1428 (1990). <https://doi.org/10.1007/BF00585460>
43. J. Pelleg, *Mechanical Properties of Ceramics*, vol. 213 (Springer, Cham, 2014)